



Estimating Caprock Impact on CO₂ Migration in the Gassum Formation Using 2D Seismic Line Data

Odd Andersen¹ · Anja Sundal²

Received: 22 July 2020 / Accepted: 13 May 2021 / Published online: 25 May 2021
© The Author(s) 2021

Abstract

Realizable CO₂ storage potential for saline formations without closed lateral boundaries depends on the combined effects of physical and chemical trapping mechanisms to prevent long-term migration out of the defined storage area. One such mechanism is the topography of the caprock surface, which may retain CO₂ in structural pockets along the migration path. Past theoretical and modeling studies suggest that even traps too small to be accurately described by seismic data may play a significant role. In this study, we use real but scarce seismic data from the Gassum Formation of the Norwegian Continental shelf to estimate the impact of topographical features of the top seal in limiting CO₂ migration. We seek to estimate the amount of macro- and sub-scale trapping potential of the formation based on a few dozen interpreted 2D seismic lines and identified faults. We generate multiple high-resolution realizations of the top surface, constructed to be faithful to both large-scale topography and small-scale statistical properties. The structural trapping and plume retardation potential of these top surfaces is subsequently estimated using spill-point (static) analysis and dynamical flow simulation. By applying these techniques on a large ensemble of top surface realizations generated using a combination of stochastic realizations and systematic variation of key model parameters, we explore the range of possible impacts on plume advancement, physical trapping and migration direction. The stochastic analysis of trapping capacity and retardation efficiency in statistically generated, sub-seismic resolution features may also be applied for surfaces generated from 3D data.

Keywords Gassum · CO₂ storage · Flow simulation · Stochastic modeling

Funded by the Norwegian Research Council under Grant 268512 of the CLIMIT-programme.

✉ Odd Andersen
odd.andersen@sintef.no

¹ Department of Mathematics and Cybernetics, SINTEF Digital, Oslo, Norway

² Department of Geosciences, University of Oslo, Oslo, Norway

1 Introduction

Geological sequestration of CO₂ is essential in achieving rapid and efficient reductions in anthropogenic greenhouse gas emissions, as recommended by the IPCC. Deep saline aquifers are considered to hold the largest potential storage volumes by far globally, while depleted oil and gas fields may add additional geological storage potential (Benson et al. 2005). Saline aquifers are not otherwise considered resources (i.e., uneconomical), and therefore there are generally much less data available compared to subsurface areas with prospective or depleted hydrocarbon resources. Thus, storage quality and security assessments in CO₂ storage reservoirs are often based on sparse data (i.e., seismic surveys, geo-physical well logs, rock samples).

Nevertheless, practical storage of CO₂ in saline aquifers has already been demonstrated at industrial scale, both onshore (Duong et al. 2019) and offshore (Ringrose 2018). A large share of brine-filled reservoirs relevant for CO₂ storage are *sloping*, (*semi*-)open aquifers. These are inclined, porous and permeable reservoir layers (e.g., sandstone), overlain by impermeable, confining units (e.g., shale), but with no lateral confinement, meaning that injected CO₂ can migrate gradually up dip within the reservoir along the caprock. Several of the saline aquifers off the Norwegian coast are sloping and with open or semi-open boundaries (Riis and Halland 2014). In some settings, there could be a risk for buoyant CO₂ to eventually reach the surface or seabed, at least in principle. However, the long-term risk of leakage is likely low in practical terms, both because CO₂ movement is slow relative to the long time scales involved, and because physical and chemical trapping mechanisms gradually immobilize CO₂ and retard the plume migration. In microscale (mm-m), droplets of CO₂ will be capillary trapped at narrow pore throats, some will dissolve and dissociate in water, and may eventually even mineralize, ensuring absolute immobilization of CO₂ in-situ (Bachu et al. 1994). Further, significant volumes of free-phase, buoyant CO₂ may be structurally trapped beneath the caprock surface due to meso-scale (ms to 10s of ms) irregularities (i.e., faults, undulations or folds). Predicting how this trapping mechanism may prevent CO₂ leakage or migration outside of a defined storage license is essential in risk assessment for sloping aquifer storage prospects. Open or semi-open boundary conditions may reduce the risk of pressure buildup during CO₂ injection, which is advantageous both in terms of injectivity, storage capacity and reservoir integrity.

The goal of the CO₂ Upslope project has been to investigate methods for risk assessment of sloping, (semi-)open saline aquifers where available data are scarce for practical storage of CO₂, using the Gassum Formation as a case study. The Gassum Formation is a sandstone of Late Triassic age and vast aerial extent offshore Norway and Denmark (Skagerrak) and onshore Denmark (Nielsen 2003), see Fig. 1. Reservoir grade, brine-filled layers in the Norwegian sector are located at burial depths down to ca. 3500 m below the seafloor, with an upwards sloping trend toward the north (Baig et al. 2013; Olivarius et al. 2019). The overlying Fjerritslev Formation is sealing, comprising a thick succession of mudstones and shales (Nielsen 2003). The Gassum saline aquifer is considered to be a promising candidate for CO₂ storage (Bergmo et al. 2017), although available data remain limited. While the CO₂ Upslope project has considered how several trapping mechanisms are limiting long-time migration, as well as investigated mechanisms behind near-well salt precipitation (Parvin et al. 2020), the study presented in this article focuses on the potential for faulted and undulating caprock to slow down the advancement of a CO₂ plume and trap CO₂. This is relevant for proving low risk of leakage to the seabed. The main challenge is

data scarcity, with interpretations of top reservoir and cap rock topography based solely on spatially spread-out 2D seismic line data.

The effect of caprock topography on CO₂ migration and trapping has been extensively studied in the past, both in terms of large-scale structural/stratigraphic trapping (Riis and Halland 2014; Nilsen et al. 2015a, b; Goater et al. 2013) and in terms of impact of small-scale undulations (“rugosity”) on plume advancement. Both conceptual (Gasda et al. 2012, 2013; Nilsen et al. 2016) and synthetic (Nilsen et al. 2012; Shariatipour et al. 2016) studies have shown how caprock rugosity has the practical effect of slowing down the advancing plume front. In the conceptual framework of vertical equilibrium modeling (cf. Sect. 3.2), the upscaled effect is shown to be analogous to that of a modified CO₂ relative permeability curve, reducing propagation speed for thin plume tips (Gasda et al. 2013; Nilsen et al. 2016).

Studies of the impact of caprock topography on plume migration for a hypothetical storage scenario in the Gassum Formation is complicated by the lack of 3D data. Contrary to other well-studied reservoirs such as Sleipner (Singh et al. 2010; Ringrose 2018), for which there exist a large amount of 3D seismic and other monitoring data (Equinor: Sleipner 4d seismic dataset 2019; Equinor: Sleipner 2019, benchmark model 2019), the data coverage concerning the Gassum Formation in the Norwegian sector of Skagerrak is relatively scarce, including some few 2D seismic surveys and one research well confirming the top formation. There is no hydrocarbon production in the study area, and as saline aquifers lack economic potential, data scarcity is a common challenge in reservoir characterization for CO₂ storage. Whereas it is possible to interpolate a surface between the interpreted 2D lines, such a surface will generally be smoothed and lack the fine-scale structure that is nevertheless important to evaluate plume advancement speed and depletion from small-scale structural trapping (Fig. 1, middle plot).

In addition, a large number of faults with varying displacements can be inferred from the seismic lines. Some faults are sufficiently large to be correlated between several seismic lines (Fig. 1, middle plot). Most faults are smaller scale, however, and die out between far-spaced seismic lines. Little can be known regarding the lateral extent and orientation of these faults. For clarity of discussion, we will in this article make an explicit distinction between (I) *large-scale faults*, being the regional faults that can be correlated between multiple seismic lines and (II) *intermediate scale faults*, being the faults that can be identified on a single seismic line only, but still have large enough throws (displacements) to be recognized within seismic resolution. Similarly, we use the term (III) *small-scale faults* to refer to faults too small to be recognized as such on the seismic data. Alongside with other small-scale undulations in top surface (which may be hard to distinguish from seismic noise), the latter is considered as a component of *caprock rugosity*, and will be modeled separately. For the purpose of this paper, we seek to infer as much information about the Gassum top surface as we can from the seismic lines. This includes statistical analysis to recreate small-scale topographical features through stochastic simulation, combined with a statistical model of fault sizes, distributions and shapes. By varying several unknown parameters, we are able to generate a large set of detailed surfaces which remain overall consistent with the observed data. In a second phase, we numerically simulate buoyant fluid flow up along and below these surfaces, assessing the impact of small-scale undulations and faults on long-term CO₂ migration in comparison with migration along smooth surfaces. We then analyze the result by looking at the spread of several aggregate quantities, including total structural trapping potential, plume tip advancement and plume center of mass, as well as how different choice of parameters impact these aggregates. For

Fig. 1 *Top*: Regional extent of the offshore parts of the Gassum Formation displayed in depth (m), as interpreted by Baig et al. (2013). Model area with the available 2D lines (yellow) shown in polygon (pink). *Middle*: Top surface of the Gassum Formation inside the model area, shown in TWT and interpolated (smoothed) between 2D seismic lines. Regional faults, as interpreted by Gregersen et al. (2018) and displacing the top Gassum reservoir are displayed as intersecting planes. Note that small scale undulations/faults are only represented along line data traces. *Bottom*: Example of reservoir (Gassum, yellow) and seal (Fjerritslev, gray) formation geometries shown in North-South-oriented 2D seismic line through the study area (from the SKAGRE96 survey, location marked in the regional map top left). Suggested location of CO₂ injection well shown. Buoyant fluid will migrate upwards within the reservoir, and upslope along the top reservoir/base seal, gradually becoming trapped in structural traps (faults), as well as capillary and chemically immobilized along the migration path

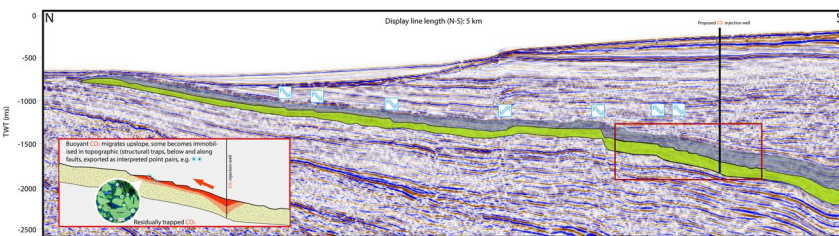
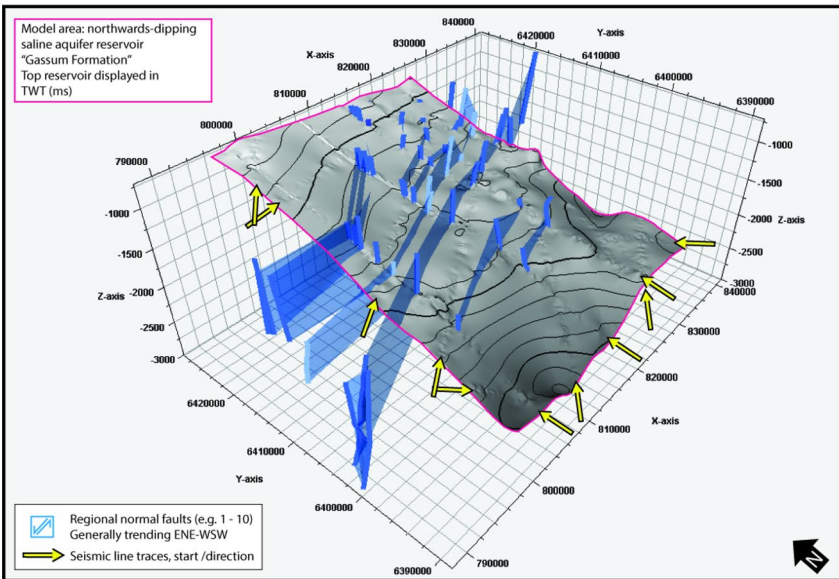
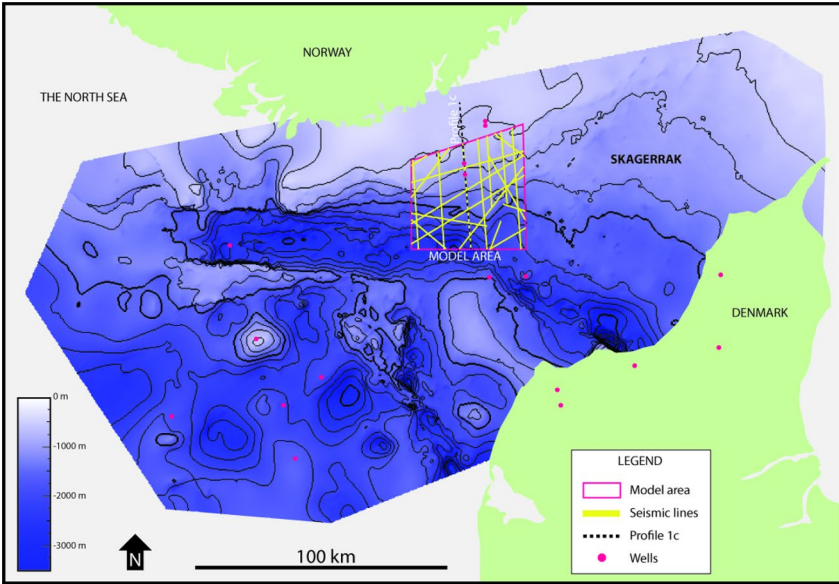
simulation and model-building, we use scripts based on the open-source Matlab Reservoir Simulation Toolkit (MRST) (The MATLAB 2019; Lie 2019).

In the flow simulation phase, several simplifying assumptions are made. In particular, only the top surface topography is considered in terms of plume retention; other trapping mechanisms are ignored. Moreover, faults are considered only in their geometric effect on the caprock topography, and we do not consider the reduction in permeability across fault planes, nor the risk of upward leakage through faults. Reservoir properties and cap rock integrity are major controls on long term CO₂ storage, and have been addressed in other studies (Olivarius et al. 2019; Nielsen 2003; Bruno et al. 2014; Springer et al. 2020). In this study, faults are considered transmissive across sand-sand contacts (Fossen and Bale 2007), and sealing along mudstone intervals (Bruno et al. 2014). While the work presented here focuses on caprock topography alone, we emphasize the importance of these other effects. Although our present study suggests that the presence of small-scale detail and a large number of small faults has the potential to slow down plume advancement by some 10-30 percent, the cumulative effect of all known trapping mechanisms and reduced fault permeability may plausibly reduce plume migration significantly more. An important risk-reducing factor at Gassum is that the sloping aquifer is open, and thus hazardous pressure build-up and fracturing is unlikely (Chadwick et al. 2008).

2 Top Surface Modeling

The first part of our study focuses on generating top surface realizations that are consistent with the input data. The data available for the study consist of 13 seismic 2D lines from 3 different seismic surveys (IKU88, FSB88 and SKAGRE96), as well as 41 fault sticks corresponding to interpreted regional faults (intersecting more than one seismic line). Regional faults have throws of more than 50 m, and are generally striking WSW-ENE. The domain of study, a four-sided polygon with an extent of 45.7 km east-west and 50.3 km north-south, was chosen to tightly fit the region of a prospective CO₂ storage site (Baig et al. 2013; Bergmo et al. 2017) covered by the seismic lines.

Regional faults (I) were imported as planes from Gregersen et al. (2018); Olivarius et al. (2019), as shown in the middle plot in Fig. 1. Intermediate scale faults (II) were interpreted as paired (displaced) points along the seismic reflector representing an acoustic impedance contrast between the sandy reservoir and shaly seal. The reflector (line data) and faults (point data) were subsequently converted from the seismic time domain (i.e., two-way travel time in m/s) to depth, using a model for the seismic velocity distribution in the overburden by Baig et al. (2013).



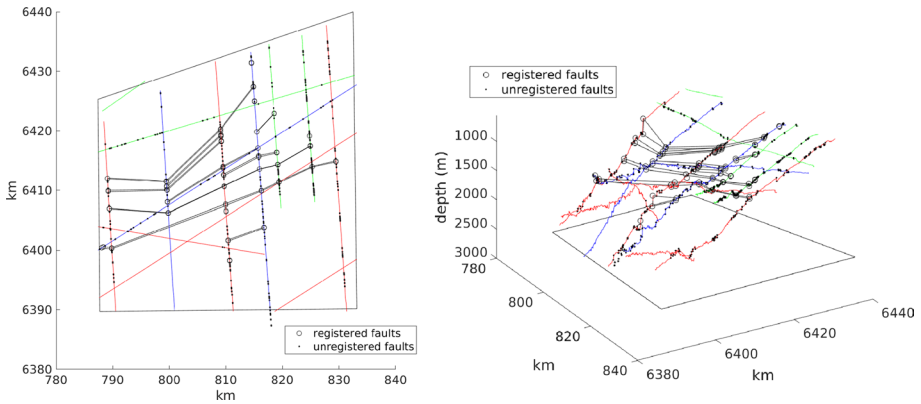


Fig. 2 Domain of study, with seismic line data and faults indicated. Colors indicate the different seismic surveys (green: IKU88, blue: FSB88, red: SKAGRE96). Circles are used to indicate where regional faults intersect the seismic lines, and the corresponding fault polygons obtained by linear interpolation (black lines). Intersections between depth-converted seismic lines and intermediate-scale faults (II) are indicated with black dots. *Left*: top view; *Right*: oblique view

As can be seen in Fig. 2, the seismic lines criss-cross the domain, but there are large areas for which no data exists. The reflector interpreted to correspond to the top Gassum Formation is irregular in all seismic lines, and cross-cut by numerous faults, i.e., fracture zones with downward displacement, i.e., normal faults, (mostly) due to large-scale, structural extension. The seismic lines can be seen on the right plot of Fig. 2, as well as in Fig. 3, where a single seismic line from the FSB88 survey is plotted in profile.

The software algorithms used for top surface modeling in this section (spline surface approximation, local correction, stochastic simulation and fault generation) have all

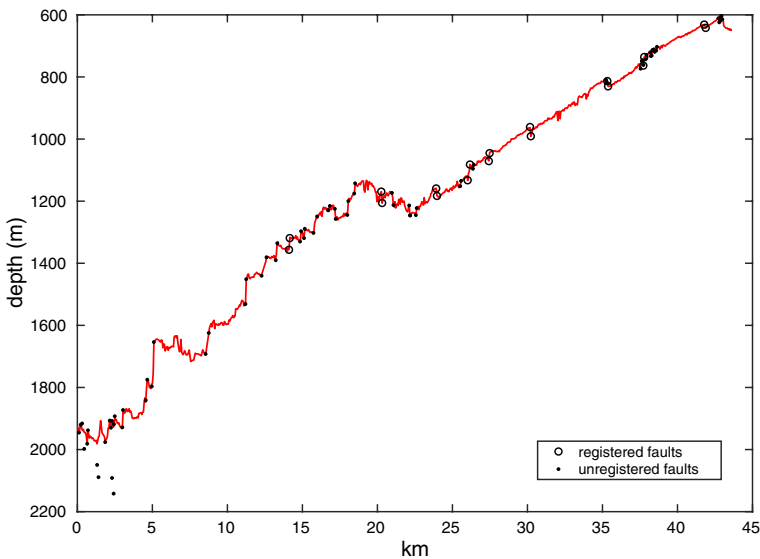


Fig. 3 Depth-converted seismic line from the FSB88 survey, profile view. Intersections with regional (I) and intermediate-scale (II) faults are indicated with circles and dots, respectively

been implemented in MRST, and are scheduled to be included as a separate module in a future release, although this has not yet happened at the time of writing of this article.

2.1 Constructing the Trend Surface

The first step is to generate a trend surface, which estimates the overall shape of the top seal topography. To this end, we use bi-cubic B-spline tensor product penalized least square surface approximation (Floater 1998; von Golitschek and Schumaker 2002). To specify the spline surface, we use a grid of 40×40 control points (degrees of freedom) and a thin-plate smoothing term weight of 10^{-8} . This choice of parameters allows us to define a surface that provides a good approximation of the input data without introducing the small-scale detail locally around the seismic lines that is seen in Fig. 1. As input data, we used all points on the seismic lines (a total of 25,703 points) after depth conversion, as well as a set of densely sampled points along the interpolated regional faults (18600 points). The resulting surface is shown on the top plot of Fig. 4.

While the surface shown in the upper plot of Fig. 4 generally provides a good approximation to the input data while avoiding local artifacts around the seismic lines, it does not resolve the sharp edge and discontinuities around regional faults. In order to include this, we generate a correction spline surface where *only* the sampled points from the fault polygons are used as input data. Instead of least square interpolation, we here use a multilevel B-spline algorithm better suited to local corrections (Lee et al. 1997), where the approximating surface remains constant (zero) away from input data. After adding the correction surface to the trend surface, we obtain the surface shown on the bottom plot of Fig. 4, where regional fault discontinuities are much better resolved.

2.2 Statistical Description of Small-Scale Detail

Since we in this study are interested in the impact of detailed caprock topography on CO₂ migration, we need to add smaller-scale detail and a representation of the intermediate scale faults (II) which cannot be correlated between seismic lines. A smooth top reservoir/seal surface is not representative of reality. The frequency, size and orientation of faults, folds or facies features (e.g., channels) should form an integral part of risk assessment, also in areas with sparse data, as the caprock topography can accelerate or decelerate plume propagation, and direct preferential migration pathways. We seek to generate plausible representations based on statistical analysis of the input data.

In Fig. 5, we compare the seismic lines to the corresponding lines drawn from the trend surface. As can be seen from the upper plot, the trend surface follows the Gassum seismic reflectors closely, but does not capture small-scale detail. The residuals are shown on the lower plot, where we note a certain spatial coherence. We consider these small-scale variations to be a combination of small-scale faults (III), other small-scale variations and seismic noise, without making any attempt to separately identify these components. We seek to extend these variations (“rugosity”) to the whole surface, so that any arbitrarily sampled seismic line would exhibit similar small-scale variations as those seen on the figure. On the other hand, we are not particularly concerned about exact interpolation of the input data, since it is the statistical nature of the small-scale topography that impacts CO₂ migration. We use the residuals seen in Fig. 5 to compute a semivariogram (Fig. 6, left), which we can subsequently use to generate stochastic realizations of a 2D Gaussian random field with

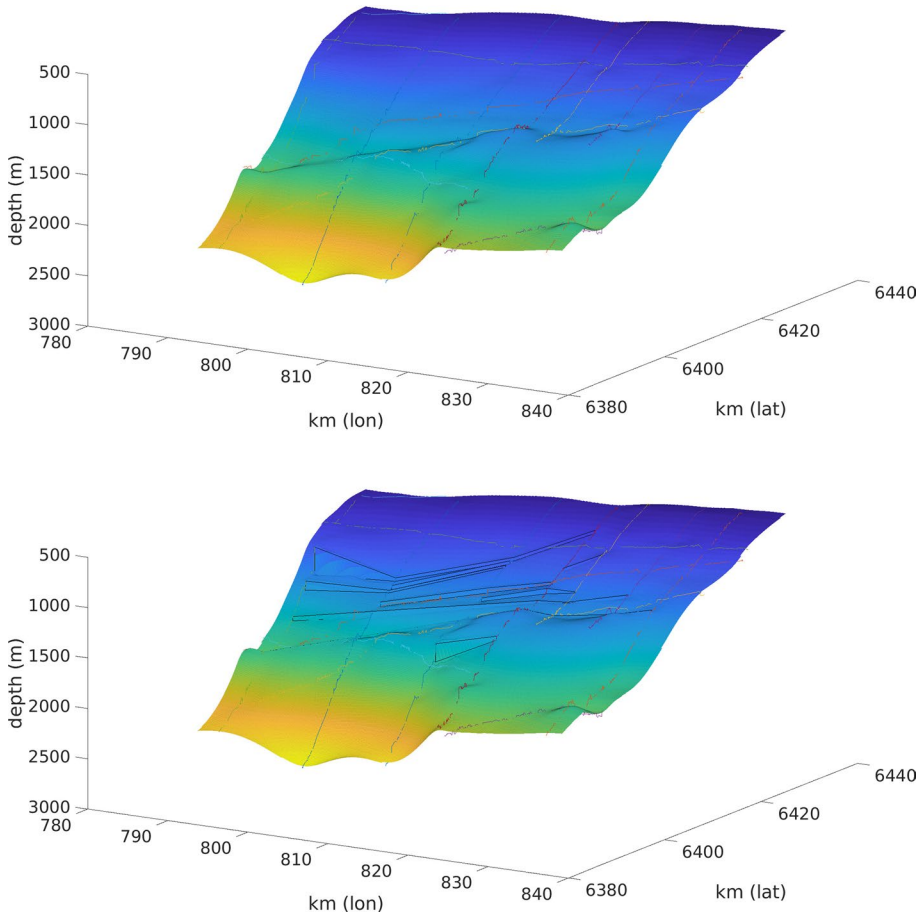


Fig. 4 Trend surface generated by least square bi-cubic spline approximation of the seismic lines and densely sampled fault polygons. The seismic lines are also shown in the plots. *Top*: basic trend surface with no local correction for regional fault edges; *Bottom*: trend surface with local correction for regional fault edges. The regional fault polygons (black) are superposed

the same spatial correlations and mean deviations as those observed in the input. One such realization is shown on the right plot of Fig. 6.

By adding a realization of this Gaussian random field to the trend surface, we obtain a surface like the one seen in Fig. 7. The small-scale detail in the seismic lines thus now extends to the whole surface.

2.3 Physical Fault Model

In order to account for the roughness induced by the large number of intermediate scale faults (II) identified in the top reservoir reflector (cf. Fig. 2), we generate a number of synthetic faults and compute their impact on top surface shape. Since little can be

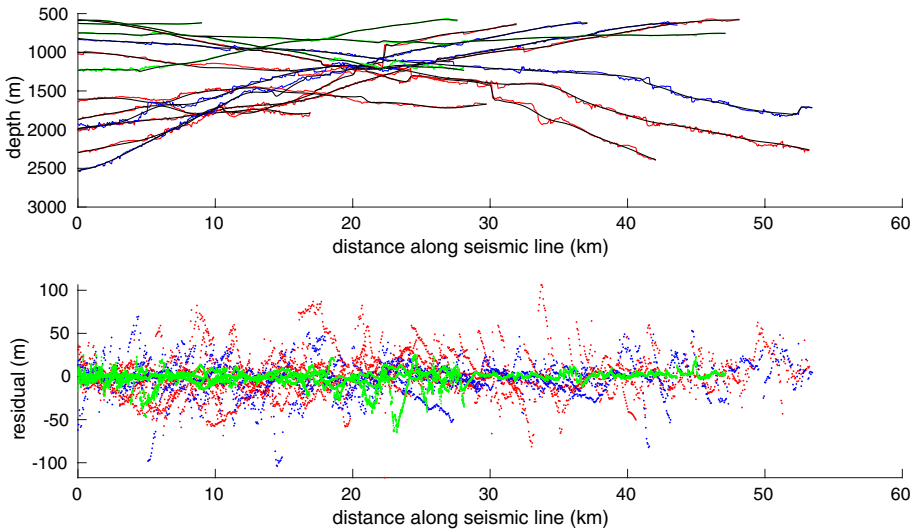


Fig. 5 *Top*: All 2D seismic lines plotted along their length. Colors indicate the individual surveys, as explained in the caption of Fig. 2. The black curves are the corresponding traces from the constructed trend surface. *Bottom*: Residuals, i.e., the differences between seismic line points and the corresponding points on the trend surface

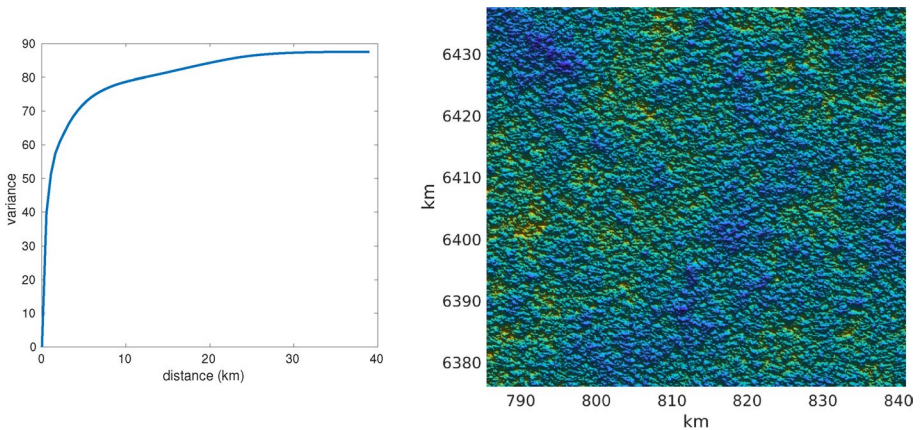


Fig. 6 *Left*: Semivariogram computed from the residuals (differences between seismic lines and trend surface). *Right*: A corresponding realization of an isotropic Gaussian random field

known about each individual fault, we seek to estimate the total number and size distribution of faults using statistical analysis.

To generate synthetic faults, we use a conceptual model proposed in Kim and Sanderson (2005), illustrated in Figs. 8 and 9. In this model, the fault slip surface is described as an ellipse with major axis length L (fault length, i.e., strike slip component) and minor axis length H (fault height, i.e., dip or normal slip component). Maximum fault

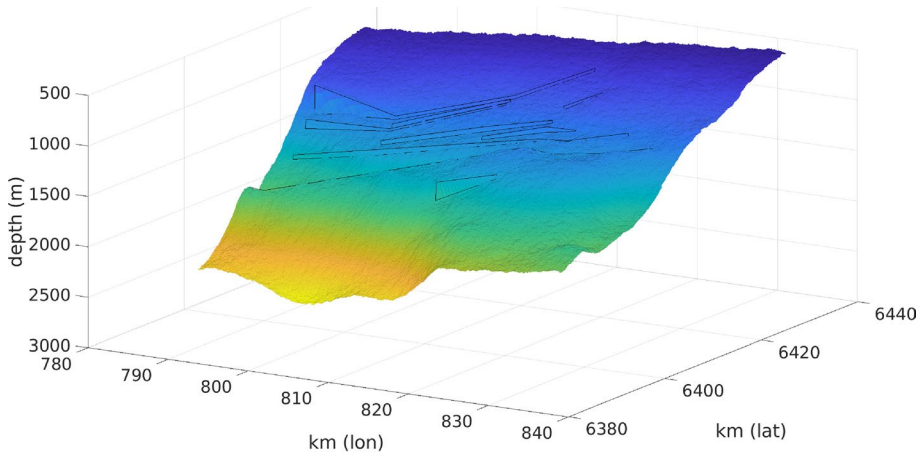


Fig. 7 Trend surface with an added realization of a Gaussian random field with same small-scale behavior as the input data

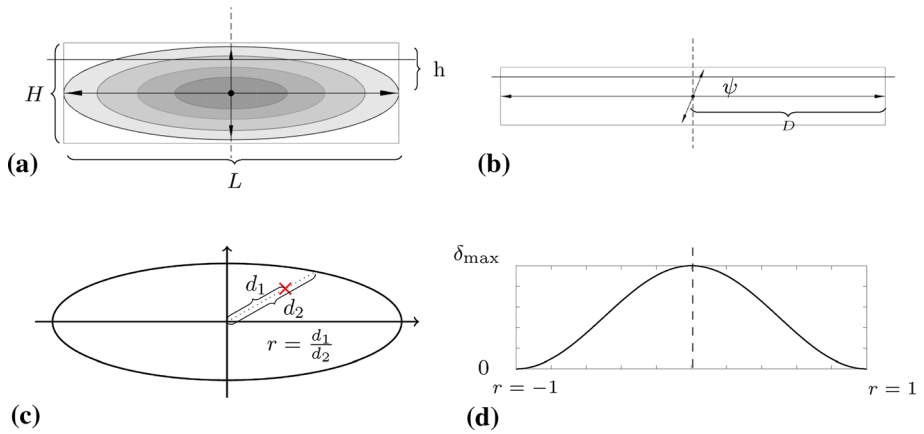
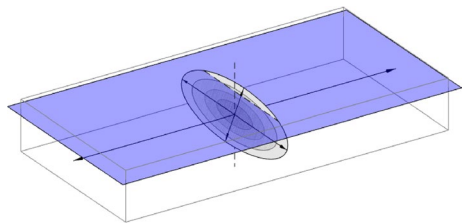


Fig. 8 Conceptual fault model. **a** Fault surface frontal view, h indicates vertical distance from Gassum top surface (horizontal line) to fault center; **b** side view (dip angle ψ); **c** definition of relative distance r from fault center to a given point x (in red); **d** displacement at the fault surface, as a function of relative distance r from fault center

Fig. 9 Oblique view of the fault surface, where the blue surface intersecting the fault represents the Gassum top surface



displacement δ_{\max} occurs at the center of the ellipse and vanishes at the boundary. To model this behavior, we assume $\delta(r) = \delta_{\max} \cdot g(r)$, with:

$$g(r) = \frac{1}{2}(1 + \cos(\pi r)) \tag{1}$$

where r is relative distance from fault center (Fig. 8c, d).

In general, the Gassum top surface will not intersect the fault directly at the fault center, but at some arbitrary vertical offset h (Fig. 8a). We consider that the fault will impact the geometry of the top surface up to a lateral distance D away from the fault plane intersection (Figs. 8b, 9).

Before using this model to stochastically generate a plausible set of faults intersecting the Gassum top surface, several parameters must be chosen:

1. The total number N of minor faults within the domain of study;
2. The size distribution of the faults;
3. The relationship between fault length L and maximal displacement δ_{\max} ;
4. The relationship between fault length L and maximum distance D of geometric impact on the top surface;
5. General fault strike;
6. Fault dip.

The total number of intermediate faults N and their size distribution (items 1 and 2) are estimated in Sect. 2.4, based on statistical analysis of the visible, interpreted faults. For the relationship between L and δ_{\max} (item 3), we use the formula (Kim and Sanderson 2005; Schultz et al. 2013):

$$\delta_{\max} = cL^n \tag{2}$$

where we use $n = 1$ (self-similarity) and $c = 0.016$, roughly in line with the statistical data presented in Kim and Sanderson (2005) for normal faults. As this is a highly uncertain parameter (Kim and Sanderson 2005; Schultz et al. 2013), we also perform a simple sensitivity analysis when running flow simulations in the second part of the paper. Sensitivity analyses are also used for item 4 and 5. For item 5 (fault strike), we use the general direction of the regional faults, which we estimate from the data to be N62°E as the base case. For item 4, we have limited information, but based on the known vertical and plane parallel displacements, we test a range of ratios D/L from 1 to 4. For fault dip, we use an average dip angle of 75°. Since the overall slope of the trend surface is about 14°, this corresponds to an average angle of 61° between fault and trend surfaces.

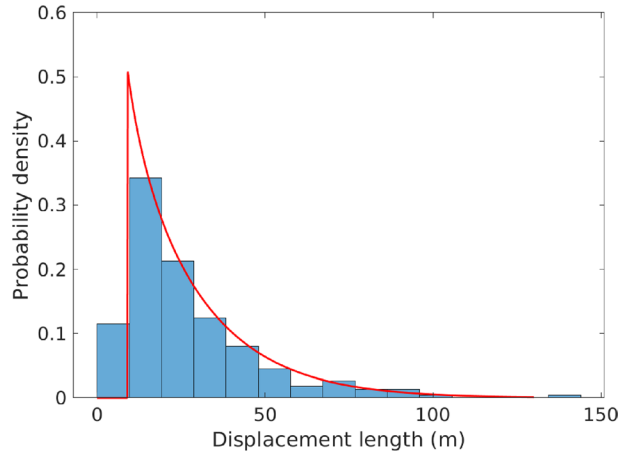
2.4 Statistical Model for Fault Size Distribution

As explained in the previous section, we consider fault displacement δ_{\max} and L to be proportional. We here assume that maximum displacement length δ_{\max} can be modeled as a random variable Δ that follows an exponential probability distribution with unknown parameter λ . Its probability density function is written:

$$f_{\Delta}(\delta_{\max}; \lambda) = \lambda e^{-\lambda \delta_{\max}} \tag{3}$$

Although there is no apriori physical argument for using the exponential distribution here, we will note that after estimating λ that this choice leads to a curve that fits the observed data quite well (c.f. Fig. 10).

Fig. 10 Histogram of measured displacement lengths of 225 intermediate faults (II), 200 of which are above $\delta_{\min} = 9\text{m}$. Bin size is 9.6m, and bars have been normalized by dividing by number of samples. The line in red shows the truncated probability distribution of Eq. (6) with $\hat{\lambda} = 0.0584\text{m}^{-1}$



In “A”, we provide detail on the derivation of formulas and how we use maximum likelihood estimation (MLE) to estimate the unknown parameter λ from the observed data. By assuming that a seismic line may intersect a fault surface at any arbitrary location, and that a line is more likely to intersect with a larger fault than a smaller one, we end up with the following formula for the probability distribution of measured fault displacement length δ interpreted from seismic reflection line data:

$$f_{\Delta_{\text{measured}}}(\delta; \lambda) = \int_{\delta}^{\infty} \frac{1}{t} f_Y\left(\frac{\delta}{t}\right) \frac{(\lambda t)^2}{2} \lambda e^{-\lambda t} dt \tag{4}$$

with:

$$f_Y(y) = \frac{2 \cos^{-1}(2y - 1)}{\pi^2 \sqrt{(1 - y)y}} \tag{5}$$

However, as noted in Kim and Sanderson (2005), limitations in the resolution of seismic data can cause observed displacements or seismic horizons below a threshold of 10 m or more to remain undetected. This is consistent with the data in our study, where the frequency of observed displacements suddenly drops below 9m, as seen in Fig. 10. For the purpose of estimating λ , we therefore work with a truncated probability distribution and exclude samples below the threshold $\delta_{\min} = 9\text{m}$. Using $\Delta_{\text{measured}}^*$ to represent “observable” measured displacements larger than δ_{\min} , we obtain the probability distribution plotted in red in Fig. 10, and defined as:

$$f_{\Delta_{\text{measured}}^*}(\delta; \lambda) = \begin{cases} 0 & \text{for } \delta < \delta_{\min} \\ \frac{f_{\Delta_{\text{measured}}}(\delta; \lambda)}{1 - F_{\Delta_{\text{measured}}}(\delta_{\min})} & \text{otherwise} \end{cases} \tag{6}$$

where we use $F_{\Delta_{\text{measured}}}$ to denote the cumulative distribution function (CDF) of Δ_{measured} . Using MLE, we finally estimate λ to be $\hat{\lambda} = 0.0584\text{m}^{-1}$.

2.5 Estimating Total Number of Intersecting Faults

In “B” we show that the number of intermediate (II) faults per unit area, N_s , can be estimated as:

$$\hat{N}_s = \frac{2c\hat{\lambda}}{\pi n_l} \sum_l \frac{B_l}{\sin \theta_l} \tag{7}$$

where n_l is the number of seismic lines, B_l is the number of fault intersections per unit length for seismic line l , $\hat{\lambda}$ as estimated above, and θ_l the angle between seismic line l and the general fault strike direction. A minor fault is counted as within a unit area if its center is located inside that area. Since we cannot detect all fault intersections for displacements smaller than δ_{min} , we only count observed fault displacements larger than this threshold when computing B_l , call the resulting estimate $\hat{N}_{measured}$, and divide its value by $1 - F_{\Delta_{measured}}(\delta_{min})$ (cf. end of Sect. 2.4) to get an estimate of the total number of minor faults per unit area (whether or not within the seismic resolution):

$$\hat{N}_{total} = \frac{\hat{N}_{measured}}{1 - F_{\Delta_{measured}}(\delta_{min})} \tag{8}$$

This procedure, when applied on our input data, gives us the estimate $\hat{N}_s = 1.945 \times 10^{-6}$ minor faults/m².

2.6 Adding Synthetic Fault Realizations to the Base Surface

Once values have been chosen for the variables in the list 1–6 in Sect. 2.4, stochastic minor fault fields can be generated. One such realization is shown in Fig. 11, generated with parameter values summarized in Table 1. The total number of fault/surface intersections within the rectangular bounding box of the model surface is obtained by multiplying N_s by total area (3.4×10^3 km²), giving a value of 6650 intersections (many of which resulting in displacements below the seismic resolution).

It should be noted that due to lack of more specific information, the spatial distribution of faults was assumed to be uniform. However, one might expect that in reality there could be a clustering of minor faults (i.e., damage zone) around the intermediate (II) and large regional (I) faults.

Table 1 Parameters used to generate fault field realization shown in Fig. 11

Parameter	Value	Comment
c	1.6×10^{-2}	Used in relation (2)
λ	$5.84 \times 10^{-2} \text{ m}^{-1}$	Parameter in exponential distribution
N_s	$1.945 \times 10^{-6} \text{ faults/m}^3$	Minor fault density
fault strike	$N62^\circ E$	$\pm 5^\circ$ std.dev. stochastic variation per fault
Fault dip	75°	$\pm 15^\circ$ std.dev. stochastic variation per fault
D/L ratio	1	c.f. Fig. 8b

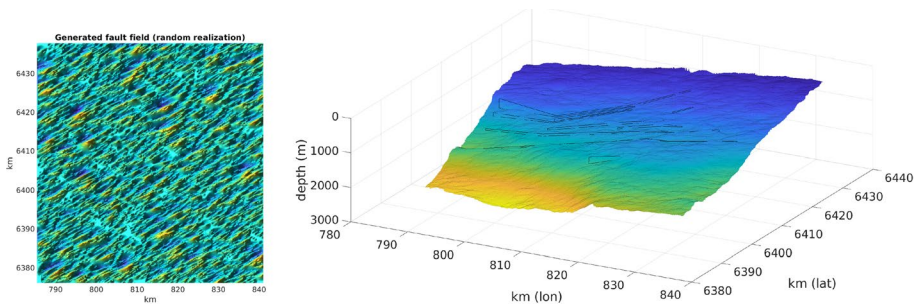


Fig. 11 *Left*: stochastically generated fault field using parameters of Table 1, shaded to enhance visibility of detail. *Right*: Generated fault field superimposed on the Gassum trend surface, also including the regional faults and small-scale detail discussed in Sect. 2.2. C.f. Fig. 7

3 Impact on CO₂ Trapping and Plume Migration

Having established a procedure to create top surface realizations with small-scale irregularities and synthetic faults, we now seek to study the impact of topography on total structural trapping capacity and long-term retardation during upslope migration of CO₂ injected into the aquifer. Although key parameters (semivariogram, N_s , λ) have been chosen to be statistically consistent with the input data, uncertainties are still considerable. Our goal is thus limited to get some rough idea of what the impact *could* be. To this end, we vary the values of c , D/L ratio and fault strike and create a large number of realizations subsequently used for analysis. We define some quantitative measures, and look at the impact of different parameters on their means and standard deviations.

Our reference set of parameters is that of Table 1, which summarizes the estimates and choices made in Sect. 2. We then introduce alternative values for c , fault strike and D/L -ratio as listed in Table 2. These are used to construct and analyze alternative sets of top surface realizations.

3.1 Impact on Structural Trapping Capacity

By “structural trapping capacity,” we refer to the total volume of topographical traps for a given top surface, regardless of trap size, and regardless of whether these traps would actually be reached by the CO₂ plume for a particular migration scenario. In order to identify the traps and compute the total trap volumes for a given reservoir top surface realization, we use the spill-point tool in MRST-co2lab (Nilsen et al. 2015). The result of this purely topographical analysis is shown in Fig. 12, where we have applied it three times: on the base surface, on the base surface with added small-scale rugosity but no intermediate (II) faults, and on the base surface with intermediate (II) faults added. (The regional faults are added beforehand as

Table 2 Alternative values for c , fault strike and D/L -ratio used for analysis in Sect. 3

c (δ/L ratio)	D/L -ratio	Fault strike
8.0×10^{-2}	2	Ref. -45°
5.0×10^{-3}	4	Ref. $+45^\circ$

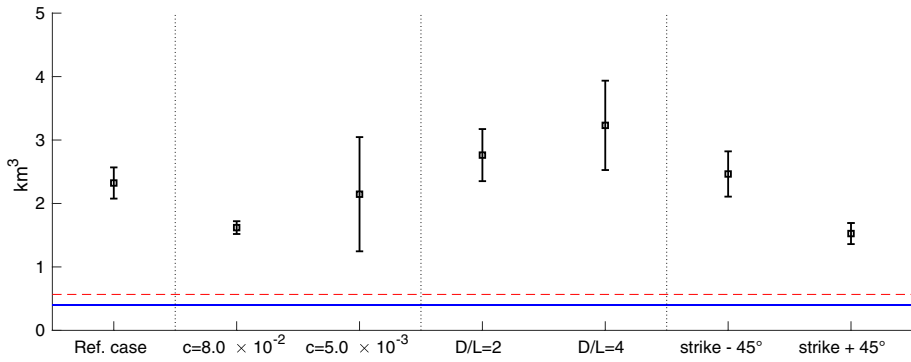


Fig. 12 Structural trapping volumes (means and standard deviations) for different choices of parameter values. Blue line: contribution of the base surface. Red line: contribution of base surface plus small scale variations. Error bars: total trapping volumes when including contribution of minor faults. Statistics are based on 30 realizations for each parameter combination

discrete features.) The reference parameter value of Table 1 was used to generate this surface realization. We see that the base surface with no added detail has only five identified traps, whereas the inclusion of small-scale variation and intermediate (II) faults adds a large number of traps of different sizes. For this particular realization, the total trap volume of the base surface is 0.40 km³, whereas that of the middle surface is 0.61 km³, and 2.1 km³ for the right surface. As such, the small-scale variations add a modest but still significant volume of structural trapping, whereas the inclusion of intermediate (II) faults increases the total trapping volume more than five-fold. It should be noted that these figures represent the total volume of the traps; in order to get the equivalent pore volumes, these values should be multiplied by the corresponding average rock porosity (in the order of 0.22 to 0.25 for the top Gassum reservoir, Ref. Olivarius et al. (2019)). These values also depend on the particular realization, although the contribution of small-scale detail remains relatively constant. The leftmost bar in Fig. 13 indicates the variations in trap volume obtained when running 30 realizations of the top surface generated using the reference parameters.

We now assess the impact of varying the parameters in Table 2. We generate another 30 realizations for each of the six alternative parameter values in the table, while holding the other parameters at their reference values (Table 1). In the second column of Fig. 12 and the left column of Fig. 14, we see the result of varying c , the ratio between maximum fault displacement δ_{max} and fault length L . Since the distribution of δ_{max} remains fixed, smaller values of c correspond to fewer but longer faults, c.f. Eqs. (2) and (7). We can observe this on the left column of Fig. 14, where the upper plot represents a “large” value

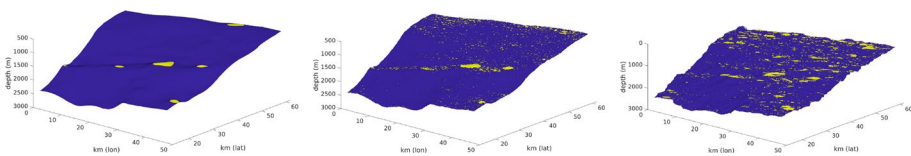


Fig. 13 Structural traps (yellow) for a top surface realization using the reference set of parameter values. *Left*: base surface; *Middle*: base surface with small-scale variations; *Right*: base surface with small-scale variations and minor faults

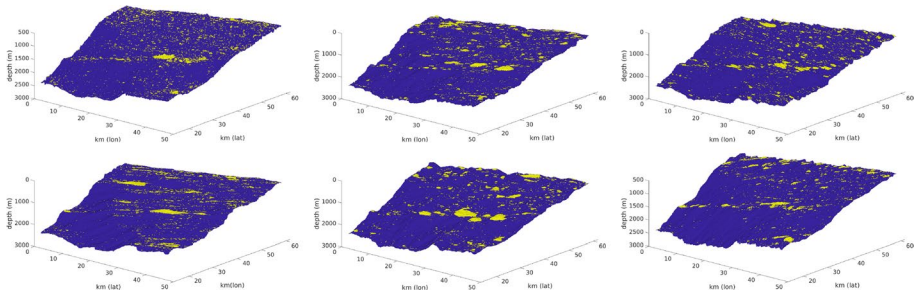


Fig. 14 Structural traps (yellow) for top surface realizations based on the alternative choices of parameters shown in Table 2 (varying one parameter at a time, keeping others at reference values). *Left*: variations in c ; *Middle*: variations in D/L -ratio; *Right*: variations in strike. Upper and lower rows correspond to the upper and lower rows of Table 2

of $c = 8.0 \times 10^{-2}$ and the lower plot a “small” value of $c = 5.0 \times 10^{-3}$. The corresponding total trapping volumes (means and standard deviations) are indicated in the second column in Fig. 12. For the “small” value of c , the few but large traps yields a high standard deviation, whereas the “large” value of c yields a very small standard deviation—the effect of a large number of small traps means that variations tend to cancel out. As such, the contribution of the fault field becomes more like that of the small-scale variations.

In the reference case, we kept the D/L -ratio to 1, which means that a fault perturbs the top surface up to a distance from the fault equal to the fault length L . This is a somewhat artificial ratio that follows from the definition of the synthetic fault geometry. As such, one might hope that this ratio would not impact the result too much, but from the third column of Fig. 12 and the second column of Fig. 14 we see that increasing this value also increases the estimated total trap volume. This highlights that results from this type of study must be interpreted with proper caution, as particularities of the synthetic fault model can (and do) influence the result.

Another uncertain parameter is the general strike direction of intermediate faults (II). When varying this value $\pm 45^\circ$ from its reference value, we get the results seen in the right columns of Figs. 12 and 14. It is clear that this angle plays a significant role with regards to structural trapping capacity, as is to be expected. The more this angle is aligned with the general upslope direction, the less the impact of the intermediate (II) faults on structural trapping becomes.

3.2 Impact on Migration

To study the impact of the top surface on long-term plume migration, we run numerical simulations using the vertical equilibrium (VE) flow simulation functionality in MRST-co2lab (Andersen et al. 2016). The assumption of VE entails that the two phases (brine and CO_2) are considered to be in hydrostatic equilibrium in the vertical direction at all times. The known vertical distribution of fluids allows upscaled flow simulations to be run on a 2D domain, with 3D reconstruction as a post-processing step. The elimination of the vertical dimension from the upscaled flow equations drastically reduces computational requirements, allowing for practical simulations on lateral high resolution grids within reasonable computational time even on standard laptops. VE can be considered a reasonable modeling assumption when vertical fluid segregation occurs on a timescale much shorter than the

timescale of interest, which is frequently the case when studying CO₂ migration in a saline aquifer. Several past studies have shown the suitability of VE-based simulation for such cases (Bandilla et al. 2019; Nilsen et al. 2011).

We first study how top reservoir topography impacts CO₂ migration injected at three different locations (southwest, south, and southeast within the domain), and for different selections of top surface realizations. We first run the simulations on grids where the top surface is set to the trend surface with no added detail (cf. Fig. 4). We then run the simulations again three times on grids where small-scale detail has been added, based on three different realizations of Gaussian random fields based on the semivariogram estimated in Sect. 2.2. Finally, we run the simulations again another three times on grids where three different realizations of intermediate (II) fault fields have been added, using the parameters of Table 1. We then compare the results across injection points and top surface type.

As we focus on the impact of the top surface itself, we employ simple, homogeneous rock parameters (permeability and porosity) and uniform vertical thickness throughout the simulated domain, chosen to be within the range estimated in Gregersen et al. (2018); Olivarius et al. (2019). It should be noted that in reality, the presence of a large number of small (III) and intermediate (II) faults would probably introduce significant local variations in effective parameters. Dissolution would likely also play an important role at the timescale studied, but is not included in the analysis below.

Table 3 lists key simulation parameters. Brine density and viscosity are kept constant, whereas CO₂ properties are functions of local temperature and pressure, following (Span and Wagner 1996; Fenghour et al. 1998).

The shape and position of the free CO₂ plume at year 500 for the different simulations is shown in Fig. 15. From these plots, we see that adding small-scale detail (row 2–4) appears to have some limited impact on the advancement of the plume compared to the smooth base case (row 1), and the plume is visibly more irregular. The actual realization does not seem to matter much; the plumes in row 2–4 are all fairly similar. When minor faults are added in (row 5–7), the plumes become more fragmented, with quite significant variation between realizations.

In order to assess the impact quantitatively, we define the following three indicators: (1) maximum distance from injection point to plume tip; (2) distance from injection point to plume center of mass; and (3) direction of migration (direction of center of mass from injection point, with 90° being north). We plot the value of these indicators as a function of time for all simulated scenarios. The graphs are presented in Fig. 16. From these plots, a few observations can be made.

Table 3 Parameters used for the simulated CO₂ migration scenarios in Sect. 3

Permeability	300 mD
Porosity	0.25
Temperature	35° C
Pressure	Hydrostatic
Brine viscosity	0.8 cP
End-point saturations (CO ₂ and brine)	0.15
Injection time	30 years
Injection rate	3 MT/year
Migration time	470 years
Top surface grid resolution	500 × 500 cells

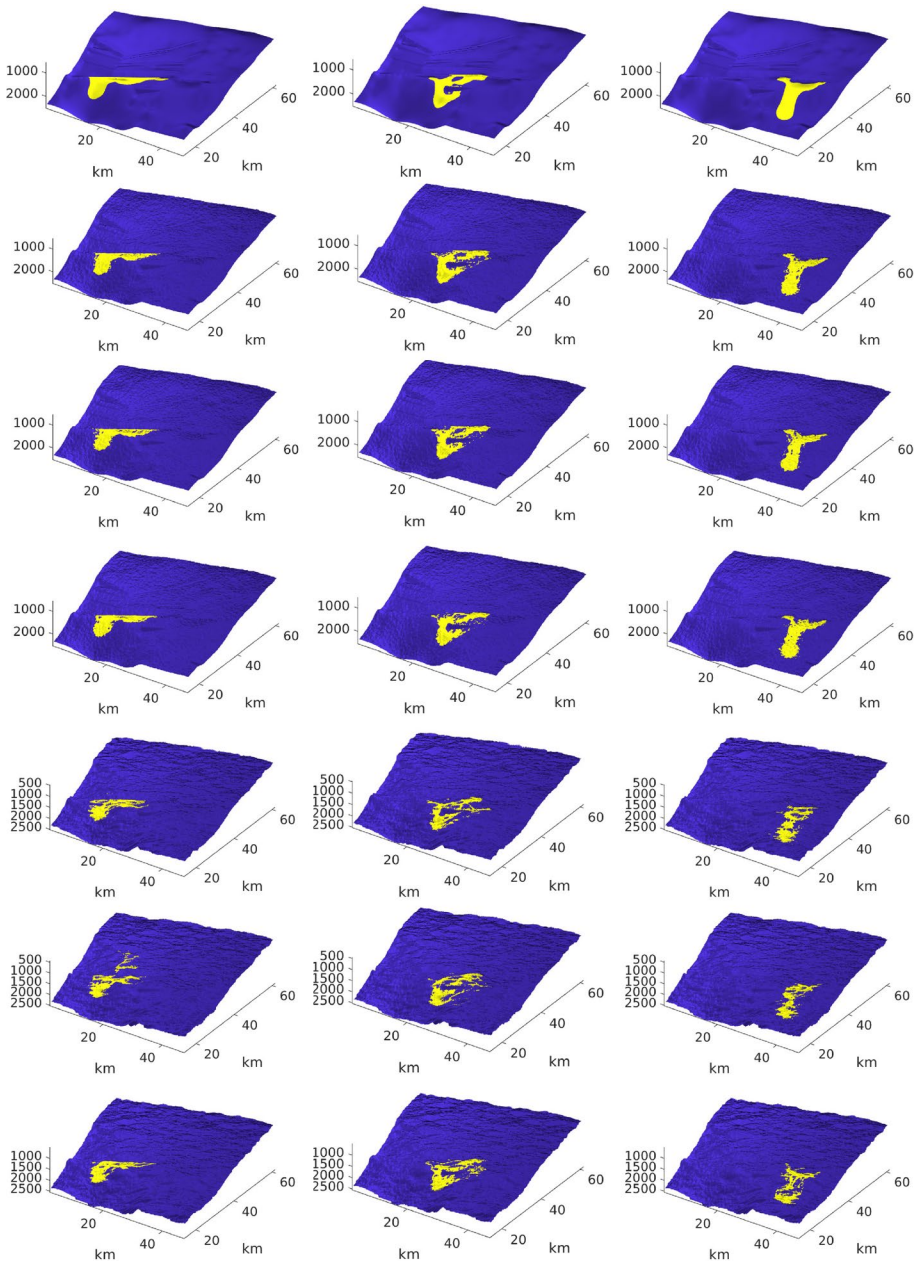


Fig. 15 Simulated outline of free CO₂ plume after 500 years of migration for three different injection locations: southwest (left column), south (middle column) and south east (right column). The rows represent different choices of top surface. The top row: the basic trend surface without added detail. Row 2–4: three different realizations of small-scale detail (Gaussian random field) added to trend surface. Row 5–7: three different realizations of intermediate faults (II) and small-scale detail added to trend surface

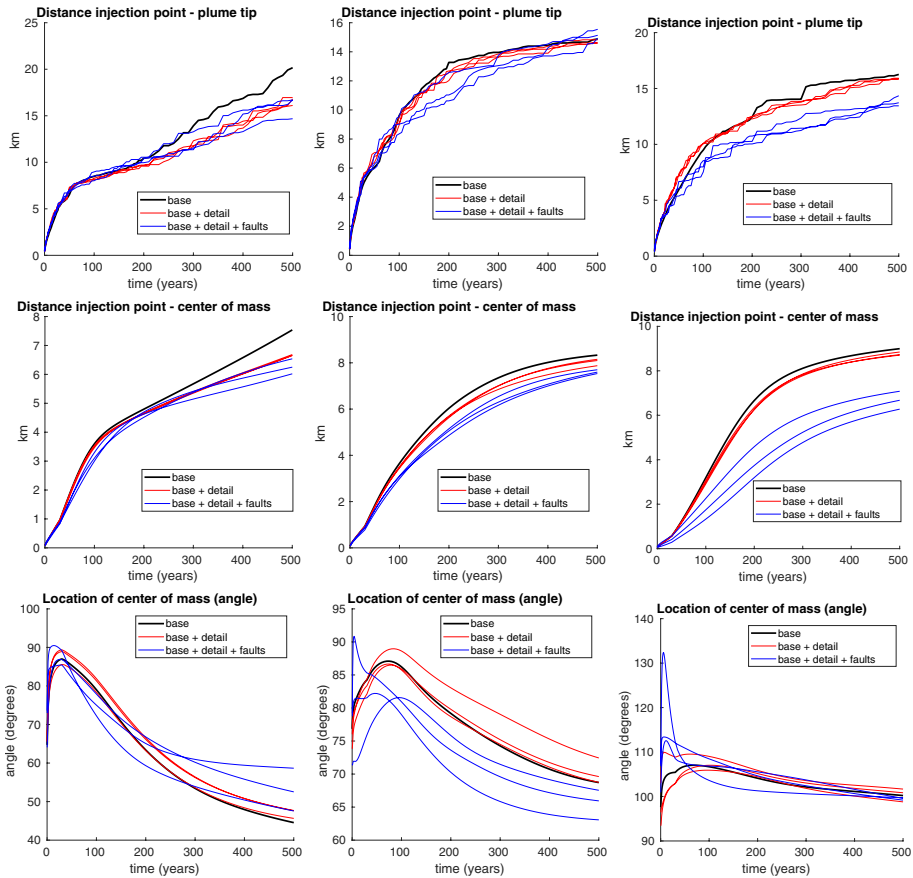


Fig. 16 Distance from injection point to plume tip (top row), from injection point to plume center of mass (middle row), and location of plume center of mass as angle from injection point ($90^\circ = \text{north}$) (bottom row). Indicators are plotted as functions of time for each of the three injection points (left: southwest, middle: south, right: southeast), and for the different types of top surface (black: only trend surface; red: trend surface with added small-scale detail; blue: trend surface with added small-scale detail *and* minor faults)

- Small-scale detail (red curves) had a very small impact on plume advancement for the south and southeast injection points. For the southwest injection point, the scenarios with small-scale detail saw a reduction in plume advancement (whether measured at tip or at center of mass) of about 15 percent. It is worth noting that migration from the southwest migration point occurs along a narrow sloping ridge (cf. Fig. 15). With the exception of one particular realization, small-scale detail had very minor impact on migration directions for all injection points.
- With the exception of the above-mentioned outlier, there was very little difference in outcome between realizations in terms of small-scale detail—the red curves match each other closely. It is not clear why one realization caused a deviation of about 4° in migration direction.
- For the top surfaces with added minor faults (blue curves), plume advancement was reduced by 0 to 30 percent depending on injection location and whether the tip or the center of mass was used as a measure. Deviations in migration direction of up to 18°

(southwest injection point) and 6° (south injection point) were seen, whereas migration direction for the southeast well remained unaffected.

While the number of samples is low (three realizations for small-scale detail and another three for minor faults), the results suggest the impact of these features on plume migration distance and direction depends significantly on the injection location. It does not seem possible here to define any globally valid top surface retardation factor.

To examine the sensitivity of the outcome to variations in the key parameters listed in Table 2 we run another set of simulations focusing on the middle well. We run a batch with 30 simulations of the reference case, for different top surface realizations. We then run six batches with 30 simulations each, where we vary one parameter at a time, for the alternative values listed in Table 2. In total, we run 210 simulations. We then plot the graphs of the indicators defined above (tip migration distance, center of mass migration distance and migration direction) in terms of batch averages and batch mean deviations, as shown in Fig. 17.

The impact of variations in c is shown in the left column on the figure. We see that the average impact on plume migration distances is not much affected, although the “small” value of $c = 5.0 \cdot 10^{-3}$ (representing average fault lengths 3.2 times longer than

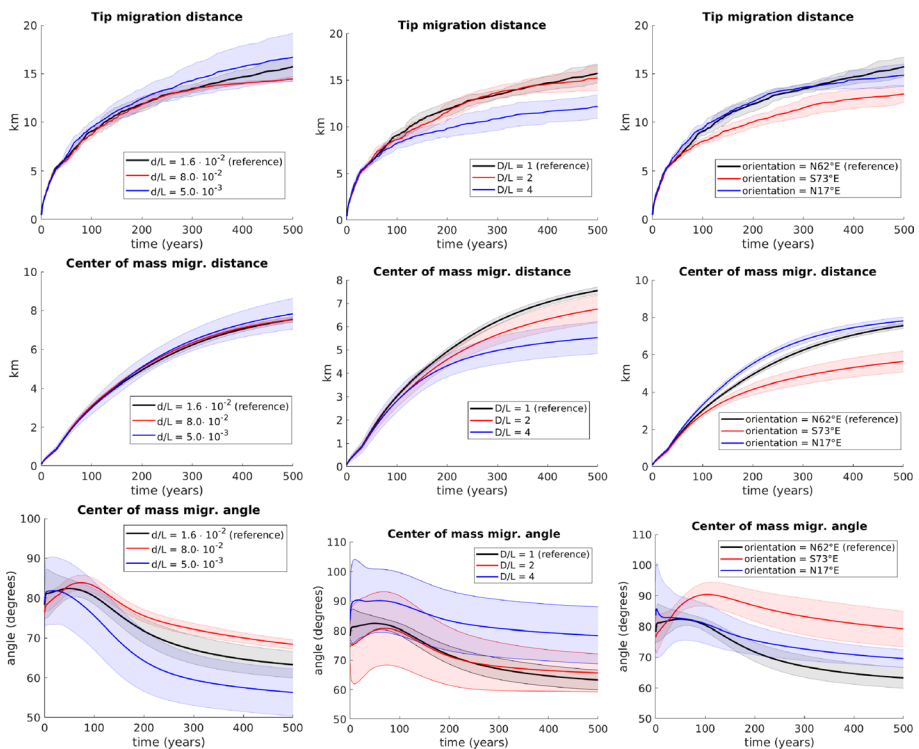


Fig. 17 Averages (solid lines) and standard deviations (shaded areas) of tip migration distances, center of mass migration distances and center of mass migration directions, for batches of 30 simulations each. Each batch represents a particular variation of one of the parameters $c = \delta/L$ (left column), D/L (middle column) and fault orientation (right column). The batch parameter value is indicated by the color, as indicated by the legends. The color black represents the reference case

the reference case) show significant variation between outcomes. The migration direction, however, seems to be significantly impacted by variations in c , where longer faults leads to stronger deviations (and more spread in outcomes). Note that the orientation of the faults, N62°E, corresponds to an angle of 28° on these plots.

In the middle column of Fig. 17, we see that increasing the value of D/L significantly decreases migration distances and reduces the eastwards deviation of plume migration. As this is an “artificial” parameter used with our synthetic fault model, these results serve as a reminder that our study is sensitive to the specifics of our fault model and should therefore be interpreted with due caution.

The right column of the figure shows the impact of varying the average orientation of minor faults. The plots confirm that minor fault orientation may have significant influence on the plume migration direction, as well as (in the S73°E case) migration distance.

4 Conclusion

In this study, we set out to assess how smaller-scale features in top surface topography may impact long-term migration of CO₂ in the Gassum aquifer, based on a set of interpreted 2D seismic lines with small-scale variations and a large number of identified minor faults. When generating top surface realizations, rather than trying to interpolate the lines exactly, we sought to create surfaces whose small-scale detail were statistically consistent with the behavior observed in the lines. With the limited amount of input data, and a number of model assumptions and highly uncertain estimates, it is not possible to say anything definite in terms of potential trapping capacity or quantified impacts on plume migration distances and orientations. Nevertheless, we believe that our results may provide some general understanding in terms of possible magnitude and behavior of these effects. In particular, our study suggests that the topographical effects of smaller-scale features and faults on plume migration depends significantly on the injection point, i.e., its location with respect to larger features in the trend surface. Consequently, it might not be possible to define universal, global “retardation factors” that predicts plume retardation from the statistical nature of smaller-scale features alone. For instance, the impact on migration from the southwest injection point (where CO₂ is funneled northeastward up a narrow ridge) is notably different from the other injection points. Our sensitivity studies also suggest that average length and orientation of minor faults can play a significant role in directing and/or slowing down CO₂ migration. It would therefore be particularly useful to be able to deduce these characteristics from monitoring data. In any case, testing the effect of intermediate scale geological features on structural trapping capacity and potential for plume retardation (e.g., fault strike perpendicular to updip, buoyant migration) or the formation of preferential flow paths (e.g., fault strike parallel with updip, buoyant migration) should be an integral part of risk assessment.

We note that our synthetic fault model introduces effects on its own. This comes from the way faults are inserted in the trend surface as a post hoc modification, which requires specification of a specific “distance of influence,” D/L . An alternative would be to include minor faults directly in the same way as regional faults are defined, using local corrections based on the multilevel B-spline algorithm (Lee et al. 1997) or something similar. Computationally, this would be a costlier option and was not attempted in this study, although it may be a worthwhile idea to pursue in the future.

Finally, we would like to reemphasize that our study focuses on the impact of small-scale caprock features, and many other important factors impacting plume development have been left out. Aquifer heterogeneities, dissolution, residual trapping, loss of permeability from salt precipitation and upward leakage through faults are all factors that could likely have first-order effects on plume development. We believe, however, that by keeping the modeling simple, the impact of caprock shape can be more easily discerned and understood.

Appendix

A Estimating Fault Displacement Distribution Parameter λ

We here present how maximum likelihood estimation was used to estimate the λ from the observed data (fault displacement lengths along seismic lines), assuming that maximum fault displacement δ_{\max} is a random variable Δ following the exponential distribution:

$$f_{\Delta}(\delta_{\max}; \lambda) = \lambda e^{-\lambda \delta_{\max}} \tag{9}$$

When doing the estimation, we need to account for the following issues:

1. A seismic line will generally not intersect a fault at its center (where displacement is δ_{\max}), but at some random relative distance r from it. The definition of r is illustrated in Fig. 8c.
2. Considering a spatial volume V filled with faults following some given size distribution, a seismic line passing through V is more likely to intersect with the surface of a larger fault than that of a smaller one.
3. Displacements close to or smaller than seismic precision will be hard to distinguish from noise and might remain unidentified in the seismic interpretation.

In order to account for (1), we introduce the random variable R to model the relative distance from the fault center to the intersection point with the seismic line. A value 0 corresponds to an intersection at the center of the ellipse, and a value of 1 to an intersection at the boundary (c.f. Fig. 8c). Assuming that any point on the ellipse is equally likely to be the intersection point, R will follow a law with probability distribution f_R :

$$f_R(r) = 2r \quad , \quad r \in [0, 1] \tag{10}$$

The displacement value at relative distance r from the center of a fault with maximum displacement δ_{\max} is given by multiplying δ_{\max} with Eq. (1). The transformation of R with (1) leads to a new random variable Y , such that $\delta_{\max} Y$ represents the fault displacement measured at an unknown intersection point for a fault with maximum displacement δ_{\max} . The transformation gives us the following probability distribution function for Y :

$$f_Y(y) = \frac{2 \cos^{-1}(2y - 1)}{\pi^2 \sqrt{(1 - y)y}} \tag{11}$$

Going one step further, we no longer consider a fault with a known maximum displacement δ_{\max} , but consider δ_{\max} to be given by a random variable Δ' with probability density

function $f_{\Delta'}(\delta_{\max}; \lambda)$ whose exact form we will proceed to determine. The measured displacement at the intersection is thus the random variable $\Delta_{\text{measured}} = \Delta' \times Y$, whose probability distribution becomes:

$$f_{\Delta_{\text{measured}}}(\delta; \lambda) = \int_{\delta}^{\infty} \frac{1}{t} f_Y\left(\frac{\delta}{t}\right) f_{\Delta'}(t, \lambda) dt \tag{12}$$

Although we assume that fault displacements and sizes follow an exponential distribution, the same cannot be said of faults intersecting with a given seismic line l . It is natural to assume that the probability of l intersecting a given fault surface will be directly proportional to the fault surface area (issue 2 in the list above). What the random variable Δ' represents is therefore the maximum displacement of a fault, *conditioned on the fact that it was intersected by the seismic line*. To derive the corresponding probability distribution $f_{\Delta'}(\delta_{\max}; \lambda)$, we apply Bayes' theorem, and write $I(l)$ to represent the situation where the fault is intersected by l :

$$P(\Delta' < \delta_{\max}) = P(\Delta < \delta_{\max} | I(l)) = \frac{P(I(l) | \Delta < \delta_{\max})}{P(I(l))} P(\Delta < \delta_{\max}) \tag{13}$$

Since our assumption is that the probability of a fault intersecting l is proportional to its area (and thus proportional to its squared length), the probability that a fault with max displacement δ_{\max} will intersect l can be written on the form $c\delta_{\max}^2$, where c is some constant. For an arbitrary fault with unknown δ_{\max} therefore have:

$$P(I(l)) = c \int_0^{\infty} \delta^2 f_{\Delta}(\delta; \lambda) d\delta \tag{14}$$

Likewise, for the conditional probability $P(I(l) | \Delta < \delta_{\max})$, we have:

$$P(I(l) | \Delta < \delta_{\max}) = c \int_0^{\delta_{\max}} \delta^2 \frac{f_{\Delta}(\delta; \lambda)}{F_{\Delta}(\delta_{\max}; \lambda)} d\delta \tag{15}$$

where $F_{\Delta}(\delta_{\max}; \lambda) = \int_0^{\delta_{\max}} f_{\Delta}(\delta; \lambda) d\delta$ is the cumulative distribution function (CDF) of the random variable Δ . Considering that by definition we also have $P(\Delta < \delta_{\max}) = F_{\Delta}(\delta_{\max}; \lambda)$, we insert (14), (15) and (9) into (13), and obtain:

$$P(\Delta' < \delta_{\max}) = \frac{\int_0^{\delta_{\max}} \delta^2 f_{\Delta}(\delta; \lambda) d\delta}{\int_0^{\infty} \delta^2 f_{\Delta}(\delta; \lambda) d\delta} = 1 - e^{-\lambda \delta_{\max}} \left(\frac{1}{2} (\lambda \delta_{\max})^2 + \lambda \delta_{\max} + 1 \right) \tag{16}$$

Since (16) is the CDF of Δ' , we obtain $f_{\Delta'}(\delta_{\max}; \lambda)$ by differentiation:

$$f_{\Delta'}(\delta_{\max}; \lambda) = \frac{d}{d\delta_{\max}} [P(\Delta' < \delta_{\max})] = \frac{(\lambda \delta_{\max})^2 \lambda e^{-\lambda \delta_{\max}}}{2} \tag{17}$$

Combining (17) with (12) and (11), we obtain the complete expression for $f_{\Delta_{\text{measured}}}(\delta; \lambda)$.

The last adjustment we need to make before estimating λ is to account for the fact that fault displacements below a certain threshold might not be identified in the seismic data due to limited resolution (item 3 on the list above). This is discussed in Sect. 2.4, where the truncated probability distribution $f_{\Delta_{\text{measured}}}(\delta; \lambda)$ is introduced in Eq. 6. It is this truncated distribution we use for the MLE estimation, along with all observed fault displacements larger than the lower threshold of $\delta_{\min} = 9\text{m}$. The MLE algorithm, which

searches for the value of λ that optimizes the likelihood of the observed data, gives the estimate $\hat{\lambda} = 0.0584\text{m}^{-1}$.

B Estimating Total Number of Minor Faults

We here aim to show how Eq. (7) was derived. We start by assuming a seismic line \mathcal{L} projected on a geological horizon of infinite extent. The horizon is intersected with faults of varying sizes, all having the same strike direction at angle θ with the seismic line (Fig. 18). We further assume that the size of the faults follow an exponential distribution (9) with smaller faults being far more frequent (they also occur associated with larger faults, in the damage zone), and we have aligned the coordinate system so that \mathcal{L} passes through the origin and is aligned with the y axis. We aim to establish a relation between the average number N_s of fault-horizon intersections per unit area and the average number N_l of faults intersected by \mathcal{L} per unit length.

The first step is to establish the distribution of fault intersection lengths with the geological horizon. We use the fault model described in Sect. 2.3 and illustrated in Fig. 8. The relationship between fault length and displacement is described by Eq. (2), where we use $n = 1$. Although faults sizes in the 3D domain are assumed to follow an exponential distribution, the same cannot be said for the faults that actually intersect with the geological horizon. The probability that a fault intersects with this surface is directly proportional to fault height, and we follow an argument similar to the one used in “A” and developed in Eqs. (13)–(17) to establish the following probability density function for maximum fault displacements Δ_l , conditioned on the fault intersecting the horizon:

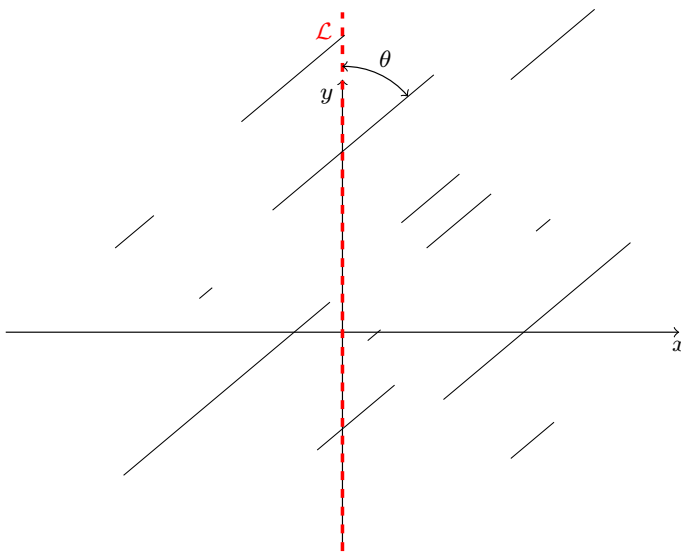


Fig. 18 Zenith view of a seismic line l (in red) traced on a geological horizon intersected by a number of minor faults (black diagonal lines), at angle θ with l . We have here chosen our coordinate system to make l coincide with the y -axis

$$f_{\Delta_I}(\delta_{\max}, \lambda) = (\lambda \delta_{\max}) \lambda e^{-\lambda \delta_{\max}} \tag{18}$$

As illustrated in Fig. 8a, we consider that a given fault will intersect with the horizon at some arbitrary vertical distance h from the fault center. If we use h_r to represent the relative vertical distance: $h_r = \frac{h}{H/2}$, then $h_r \in [0, 1]$ and for an unknown fault this value can be considered a random variable that follows uniform distribution $h_r \sim U[0, 1]$. If $L_I(h_r)$ denotes the length of the intersection between the (elliptical) fault plane and the horizontal plane as a function of h_r , we can define:

$$I(h_r) = \frac{L_I}{L} = \sqrt{1 - h_r^2} \tag{19}$$

and since $h_r \sim U[0, 1]$, we can consider $I(h_r)$ a random variable whose CDF becomes:

$$P(I < x) = 1 - \sqrt{1 - x^2} \tag{20}$$

Since we have that $L_I = Ic\Delta_I$, with c from (2), and with probability distributions for Δ_I and I obtained from (18) and (20) respectively, we obtain the CDF of L_I by integration:

$$\begin{aligned} P(l_I < x) &= \int_0^\infty P\left(I < \frac{cx}{\delta_{\max}}\right) f_{\Delta_I}(\delta_{\max}, \lambda) d\delta_{\max} \\ &= \int_0^\infty \left(1 - \sqrt{1 - \left(\frac{cx}{\delta_{\max}}\right)^2}\right) (\lambda \delta_{\max}) \lambda e^{-\lambda \delta_{\max}} d\delta_{\max} \\ &= 1 - \int_0^\infty \sqrt{1 - \left(\frac{cx}{\delta_{\max}}\right)^2} (\lambda \delta_{\max}) \lambda e^{-\lambda \delta_{\max}} d\delta_{\max} \end{aligned} \tag{21}$$

To derive this expression, we keep in mind that by definition $P\left(I < \frac{cx}{\delta_{\max}}\right) = 1$ whenever $\frac{cx}{\delta_{\max}} \geq 1$.

The second step is to estimate the average number N_I of fault intersections with the seismic line \mathcal{L} along the horizon, per unit length. We let N_s denote the average number of fault intersections with the top reservoir horizon per unit area, where a fault intersection line is considered to belong to a unit surface square if its center point is contained within the square. From Fig. 18, we see that a fault intersection line with center located at (x, y) will intersect \mathcal{L} if its length $l_I > 2\left|\frac{x}{\sin\theta}\right|$. This means that the expected (mean) number of faults intersecting \mathcal{L} per unit length is expressed:

$$\begin{aligned}
 N_l &= N_s \int_{-\infty}^{\infty} P\left(l_l > \left| \frac{2x}{\sin \theta} \right| \right) dx \\
 &= N_s \int_{-\infty}^{\infty} \int_0^{\infty} P\left(I > \left| \frac{2cx}{\delta_{\max} \sin \theta} \right| \right) f_{\Delta_l}(\delta_{\max}, \lambda) d\delta_{\max} dx \\
 &= N_s \int_0^{\infty} \left[\int_{-\alpha}^{\alpha} P\left(I > \left| \frac{2cx}{\delta_{\max} \sin \theta} \right| \right) dx \right] f_{\Delta_l}(\delta_{\max}, \lambda) d\delta_{\max} \\
 &= N_s \int_0^{\infty} \left[\int_{-\alpha}^{\alpha} \sqrt{1 - \left(\frac{2cx}{\delta_{\max} \sin \theta} \right)^2} dx \right] (\lambda \delta_{\max}) \lambda e^{-\lambda \delta_{\max}} d\delta_{\max} \\
 &= N_s \frac{\pi \sin \theta}{4c} \int_0^{\infty} (\lambda \delta_{\max})^2 e^{-\lambda \delta_{\max}} d\delta_{\max} \\
 &= N_s \frac{\pi \sin \theta}{2c\lambda}
 \end{aligned}
 \tag{22}$$

On line three of the development above, the interval of integration $(-\infty, \infty)$ was changed to $[-\alpha, \alpha]$ where $\alpha = \frac{\delta_{\max} \sin \theta}{2c}$, since by definition $P(I > x) = 0$ for $x > 1$.

Given an estimate of \hat{N}_l , we can estimate N_s as:

$$\hat{N}_s = \hat{N}_l \frac{2c\hat{\lambda}}{\pi \sin \theta}
 \tag{23}$$

Since N_l can be estimated by counting observed fault intersections in each available seismic line, dividing by the line length and averaging over the number of seismic lines, we get the following estimator for \hat{N}_s :

$$\hat{N}_s = \frac{2c\hat{\lambda}}{\pi n_l} \sum_l \frac{B_l}{\sin \theta_l}
 \tag{24}$$

where n_l is the number of seismic lines, B_l the number of fault intersections per unit length for seismic line l , $\hat{\lambda}$ as estimated in "A" and θ_l the angle between seismic line l and the general fault strike direction.

Acknowledgements This collaboration and work was performed in the CO2-Upslope project (<https://www.mn.uio.no/geo/english/research/projects/upslope/>), and the authors would like to acknowledge the Norwegian Research Council for funding under grant 268512 in the CLIMIT-programme. Further, we thank Dr. Irfan Baig, University of Oslo, for access to the regional map of Gassum and the velocity model, and Dr. Ulrik Gregersen, GEUS for access to his structural interpretation in Petrel. We acknowledge Schlumberger for the academic software licensing agreement with UiO allowing for use of Petrel, and thank Dr. Michel Heeremans for his support in accessing seismic and well data. We also thank Dr. Halvor Møll Nilsen and Dr. Olav Møyner, SINTEF Digital, for valuable advice and support.

Funding Open access funding provided by SINTEF AS. The research presented in this article was funded under Grant 268512 in the CLIMIT-programme of the Norwegian Research Council.

Availability of data and materials Generated surface realizations from the study can be made available by the corresponding author upon reasonable request.

Code availability The software algorithms used for top surface modeling in this section (spline surface approximation, local correction, stochastic simulation and fault generation) have all been implemented in the open-source software MRST, and are scheduled to be included as a separate module in a future release.

Declarations

Conflict of interest The authors declare that they have no conflict of interest.

Open Access This article is licensed under a Creative Commons Attribution 4.0 International License, which permits use, sharing, adaptation, distribution and reproduction in any medium or format, as long as you give appropriate credit to the original author(s) and the source, provide a link to the Creative Commons licence, and indicate if changes were made. The images or other third party material in this article are included in the article's Creative Commons licence, unless indicated otherwise in a credit line to the material. If material is not included in the article's Creative Commons licence and your intended use is not permitted by statutory regulation or exceeds the permitted use, you will need to obtain permission directly from the copyright holder. To view a copy of this licence, visit <http://creativecommons.org/licenses/by/4.0/>.

References

- Andersen, O., Lie, K.A., Nilsen, H.M.: An open-source toolchain for simulation and optimization of aquifer-wide CO₂ storage. *Energy Procedia* 86, 324–333 (2016). <https://doi.org/10.1016/j.egypro.2016.01.033>
- Bachu, S., Gunter, W., Perkins, E.: Aquifer disposal of CO₂: hydrodynamic and mineral trapping. *Energy Conversion and Management* 35(4), 269–279 (1994). [https://doi.org/10.1016/0196-8904\(94\)90060-4](https://doi.org/10.1016/0196-8904(94)90060-4)
- Baig, I., Aagaard, P., Sassier, C., Faleide, J.I., Jahren, J., Gabrielsen, R.H., Fawad, M., Nielsen, L.H., Kristensen, L., Bergmo, P.E.: Potential triassic and jurassic CO₂ storage reservoirs in the skagerrak-kattegat area. *Energy Procedia* 37, 5298–5306 (2013). <https://doi.org/10.1016/j.egypro.2013.06.447>
- Bandilla, K.W., Guo, B., Celia, M.A.: A guideline for appropriate application of vertically-integrated modeling approaches for geologic carbon storage modeling. *Int. J. Greenhouse Gas Control* 91, 102808 (2019). <https://doi.org/10.1016/j.ijggc.2019.102808>
- Benson, S.M., et al.: Underground geological storage. In: IPCC Special Report on Carbon Dioxide Capture and Storage, chap. 5. Intergovernmental Panel on Climate Change, Cambridge University Press, Cambridge, UK (2005)
- Bergmo, P., Emmel, B., Anthonsen, K., Aagaard, P., Mortensen, G., Sundal, A.: Quality ranking of the best CO₂ storage aquifers in the nordic countries. *Energy Procedia* 114, 4374–4381 (2017). <https://doi.org/10.1016/j.egypro.2017.03.1589>
- Bruno, M.S., Lao, K., Diessl, J., Childers, B., Xiang, J., White, N., van der Veer, E.: Development of improved caprock integrity analysis and risk assessment techniques. *Energy Procedia* 63, 4708–4744 (2014). <https://doi.org/10.1016/j.egypro.2014.11.503>
- Chadwick, A., Arts, R., Bernstone, C., May, F., Thibeau, S., Zweigel, P.: Best practice for the storage of CO₂ in saline aquifers-observations and guidelines from the sacs and CO₂store projects 14 (2008)
- Duong, C., Bower, C., Hume, K., Rock, L., Tessarolo, S.: Quest carbon capture and storage offset project: findings and learnings from 1st reporting period. *Int. J. Greenhouse Gas Control* 89, 65–75 (2019). <https://doi.org/10.1016/j.ijggc.2019.06.001>
- Equinor: Sleipner 2019 benchmark model (2019). <https://doi.org/10.11582/2020.00004>. <https://co2datashare.org/dataset/sleipner-2019-benchmark-model>
- Equinor: Sleipner 4d seismic dataset (2019). <https://doi.org/10.11582/2020.00005>. <https://co2datashare.org/dataset/sleipner-4d-seismic-dataset>
- Fenghour, A., Wakeham, W.A., Vesovic, V.: The viscosity of carbon dioxide. *Journal of Physical and Chemical Reference Data* 27(1), 31–44 (1998). <https://doi.org/10.1063/1.556013>
- Floater, M.S.: How to approximate scattered data by least squares. SINTEF Report No. STF42 A98013 (1998)
- Fossen, H., Bale, A.: Deformation bands and their influence on fluid flow. *AAPG bulletin* 91(12), 1685–1700 (2007)
- Gasda, S.E., Nilsen, H.M., Dahle, H.K.: Impact of structural heterogeneity on upscaled models for large-scale CO₂ migration and trapping in saline aquifers. *Adv. Water Resour.* 62, 520–532 (2013) <https://doi.org/10.1016/j.advwatres.2013.05.003>
- Gasda, S.E., Nilsen, H.M., Dahle, H.K., Gray, W.G.: Effective models for CO₂ migration in geological systems with varying topography. *Water Resources Research* 48(10) (2012). <https://doi.org/10.1029/2012WR012264>. <https://agupubs.onlinelibrary.wiley.com/doi/abs/10.1029/2012WR012264>

- Goater, A.L., Bijeljic, B., Blunt, M.J.: Dipping open aquifers—the effect of top-surface topography and heterogeneity on CO₂ storage efficiency. *Int. J. Greenhouse Gas Control* 17, 318–331 (2013). <https://doi.org/10.1016/j.ijggc.2013.04.015>
- Gregersen, U., Baig, I., Sundal, A., Nielsen, L., Olivarius, M., Weibel, R.: Seismic interpretation of a sloping offshore potential CO₂ aquifer; the gassum formation in skagerrak between norway and denmark. *Nordic Geological Winter meeting in Copenhagen* (2018)
- Kim, Y.S., Sanderson, D.J.: The relationship between displacement and length of faults: a review. *Earth-Science Rev.* 68(3), 317–334 (2005). <https://doi.org/10.1016/j.earscirev.2004.06.003>
- Lee, S., Wolberg, G., Shin, S.Y.: Scattered data interpolation with multilevel b-splines. *IEEE Transactions on Visualization and Computer Graphics* 3(3), 228–244 (1997)
- Lie, K.A.: *An Introduction to Reservoir Simulation Using MATLAB/GNU Octave: User Guide for the MATLAB Reservoir Simulation Toolbox (MRST)*. Cambridge University Press, Cambridge (2019). <https://doi.org/10.1017/9781108591416>
- Nielsen, L.H.: Late triassic-jurassic development of the danish basin and the fennoscandian border zone, southern Scandinavia. *GEUS Bull.* 1, 459–526 (2003). <https://doi.org/10.34194/geusb.v1.4681>
- Nilsen, H.M., Herrera, P.A., Ashraf, M., Ligaarden, I., Iding, M., Hermannud, C., Lie, K.A., Nordbotten, J.M., Dahle, H.K., Keilegavlen, E.: Field-case simulation of CO₂ plume migration using vertical-equilibrium models. *Energy Procedia* 4, 3801–3808 (2011). <https://doi.org/10.1016/j.egypro.2011.02.315>
- Nilsen, H.M., Lie, K.A., Andersen, O.: Analysis of CO₂ trapping capacities and long-term migration for geological formations in the Norwegian north sea using mrst-co2lab. *Comput. Geosci.* 79, 15–26 (2015). <https://doi.org/10.1016/j.cageo.2015.03.001>
- Nilsen, H.M., Lie, K.A., Andersen, O.: Robust simulation of sharp-interface models for fast estimation of CO₂ trapping capacity in large-scale aquifer systems. *Computational Geosciences* 20(1), 93–113 (2016)
- Nilsen, H.M., Lie, K.A., Møyner, O., Andersen, O.: Spill-point analysis and structural trapping capacity in saline aquifers using mrst-co2lab. *Comput. Geosci.* 75, 33–43 (2015). <https://doi.org/10.1016/j.cageo.2014.11.002>
- Nilsen, H.M., Syversveen, A.R., Lie, K.A., Tveranger, J., Nordbotten, J.M.: Impact of top-surface morphology on CO₂ storage capacity. *Int. J. Greenhouse Gas Control* 11, 221–235 (2012). <https://doi.org/10.1016/j.ijggc.2012.08.012>
- Olivarius, M., Sundal, A., Weibel, R., Gregersen, U., Baig, I., Thomsen, T.B., Kristensen, L., Hellevang, H., Nielsen, L.H.: Provenance and sediment maturity as controls on CO₂ mineral sequestration potential of the gassum formation in the skagerrak. *Frontiers in Earth Science* 7, 312 (2019). <https://doi.org/10.3389/feart.2019.00312>
- Parvin, S., Masoudi, M., Sundal, A., Miri, R.: Continuum scale modelling of salt precipitation in the context of CO₂ storage in saline aquifers with mrst compositional. *Int. J. Greenhouse Gas Control* 99, 103075 (2020). <https://doi.org/10.1016/j.ijggc.2020.103075>
- Riis, F., Halland, E.: CO₂ storage atlas of the norwegian continental shelf: Methods used to evaluate capacity and maturity of the CO₂ storage potential. *Energy Procedia* 63, 5258–5265 (2014) <https://doi.org/10.1016/j.egypro.2014.11.557>
- Ringrose, P.S.: The ccs hub in norway: some insights from 22 years of saline aquifer storage. *Energy Procedia* 146, 166–172 (2018). <https://doi.org/10.1016/j.egypro.2018.07.021>
- Schultz, R.A., Klimczak, C., Fossen, H., Olson, J.E., Exner, U., Reeves, D.M., Soliva, R.: Statistical tests of scaling relationships for geologic structures. *J. Struct. Geol.* 48, 85–94 (2013). <https://doi.org/10.1016/j.jsg.2012.12.005>
- Shariatipour, S.M., Pickup, G.E., Mackay, E.J.: Simulations of CO₂ storage in aquifer models with top surface morphology and transition zones. *Int. J. Greenhouse Gas Control* 54, 117–128 (2016) <https://doi.org/10.1016/j.ijggc.2016.06.016>
- Singh, V.P., Cavanagh, A., Hansen, H., Nazarian, B., Iding, M., Ringrose, P.S., et al.: Reservoir modeling of CO₂ plume behavior calibrated against monitoring data from sleipner, norway. In: *SPE annual technical conference and exhibition*. Society of Petroleum Engineers (2010)
- Span, R., Wagner, W.: A new equation of state for carbon dioxide covering the fluid region from the triple-point temperature to 1100 k at pressures up to 800 mpa. *Journal of Physical and Chemical Reference Data* 25(6), 1509–1596 (1996). <https://doi.org/10.1063/1.555991>
- Springer, N., Dideriksen, K., Holmstykke, H., Kjøller, C.: Capture, storage and use of CO₂ (ccus): seal capacity and geochemical modelling. technical report 2020/30 (2020). <https://doi.org/10.13140/RG.2.2.14868.73603>
- The MATLAB Reservoir Simulation Toolbox, version 2019b (2019). <http://www.sintef.no/MRST/>

The upslope project: Optimized CO₂ storage in sloping aquifers (upslope) (2017–2019). <https://www.mn.uio.no/geo/english/research/projects/upslope/>. RCN grant number 268512
von Golitschek, M., Schumaker, L.: Penalized least squares fitting. *Serdica Math. J.* **28**(4), 329–348 (2002)

Publisher's Note Springer Nature remains neutral with regard to jurisdictional claims in published maps and institutional affiliations.